Journal of Biomechanics 91 (2019) 140–150

Contents lists available at ScienceDirect

Journal of Biomechanics

journal homepage: www.elsevier.com/locate/jbiomech
www.JBiomech.com

Numerical simulation of haemodynamics of the descending aorta in the non-diabetic and diabetic rabbits

Yuanhang Zhou [a,1], Jianhua Tong [b,1,*], Xin Li [b], Xuanyu Li [c], Guixue Wang [a,*]

[a] Key Laboratory of Biorheological Science and Technology, Ministry of Education, State and Local Joint Engineering Laboratory for Vascular Implants, Bioengineering College of Chongqing University, Chongqing, PR China
[b] Shanghai East Hospital, Institute for Biomedical Engineering and Nano Science, Tongji University School of Medicine, Shanghai, PR China
[c] Shanghai Jiao Tong University and Chiba University International Cooperative Research Center, School of Naval Architecture, Ocean and Civil Engineering, Shanghai Jiao Tong University, Shanghai, PR China

ARTICLE INFO

Article history:
Accepted 13 May 2019

Keywords:
Diabetes mellitus
Descending aorta
Haemodynamics
Wall shear stress
Finite element method

ABSTRACT

Diabetes mellitus (DM) is a predisposing risk factor leading to macrovascular diseases. Changes in haemodynamics of the diabetic aortas remain largely unclear and relevant computational analyses are lacking in the literature. Ten adult rabbits (1.6–2.2 kg) were collected and the type I diabetic rabbit model was induced by injection of alloxan. A total of five control and five diabetic rabbit aortas were considered for subsequent numerical simulation. The CT scanning was performed to reconstruct three-dimensional model of the individual rabbit descending aorta. The flow velocity waveforms were measured by ultrasound machine and were set to be the inlet boundary conditions. The reconstructed aortas were then imported into ANSYS to perform mesh generation and computational analysis. Results showed that the distributions of haemodynamic indicators time-averaged wall shear stress (TAWSS), oscillating shear index (OSI) and transverse wall shear stress (transWSS) in the non-diabetic rabbit aortas were similar to those in the diabetic rabbit aortas. However, the mean values of TAWSS and transWSS in the non-diabetic rabbit aortas were significantly higher than those values in the diabetic rabbit aortas (TAWSS: $p = 0.04$; transWSS: $p = 0.02$). The back of right renal artery tended to have high OSI in both the non-diabetic and the diabetic rabbit aortas. Notably, the regions with high OSI tended to have intense disturbed flow and low TAWSS in the most diabetic rabbit aortas. The results suggest that diabetes leads to changes in haemodynamic parameters in the rabbit aortas. In particular, the lower TAWSS and the higher OSI within the diabetic aortas may further contribute to aortic wall remodeling.

1. Introduction

Diabetes mellitus (DM) is a major risk factor to cause macrovascular diseases (Bachmann and Wang, 2018; Casanova et al., 2017; Wijngaarden et al., 2017). Atherosclerosis is regarded as one of the main complications of diabetes and has significant impact on the health of diabetic patients. It has been well known that atherosclerotic plaques frequently form in the bifurcation zone and the local curved regions of the arteries (Feng et al., 2017; Lehman et al., 2009; Seftel, 2017; Xu et al., 2018; Zhao et al., 2017). Because these locations are highly susceptible to disturbed flow that may lead to changes in haemodynamic parameters. Although the diabetes-related atherosclerosis is relatively rare in the descending aorta, diabetes contributes to remodeling of the descending aorta (Akhtar et al., 2014) and impairs the elastic properties of the aortas. (Tong et al., 2018) It should be emphasized that increases in blood glucose also contribute to alterations in haemodynamics in the aorta and will directly or indirectly promote pathological changes to initiate formation of atherosclerotic lesions (Beckman et al., 2002).

It has been well known that haemodynamic parameters are important to reflect the effects of blood flow on the arterial wall. For example, wall shear stress (WSS) is the frictional force induced by the movement of blood flow on the endothelial cells (Caro et al., 1971; Malek et al., 1999). Based on WSS, haemodynamic parameters such as time-averaged wall shear stress (TAWSS), oscillating shear index (OSI) are further computed to evaluate intensity of

* Corresponding authors at: Tongji University School of Medicine, Chifeng Road 67, Shanghai 200092, PR China. Tel.: +86 21 65983706 (J. Tong). Key Laboratory for Biorheological Science and Technology of Ministry of Education, State and Local Joint Engineering Laboratory for Vascular Implants, Bioengineering College of Chongqing University, Chongqing 400030, PR China. Tel.: +86 23 65112675; Fax.: +86 23 65112672 (G. Wang).

E-mail addresses: tongjh@tongji.edu.cn (J. Tong), wanggx@cqu.edu.cn (G. Wang).

[1] These authors contributed equally to this study.

https://doi.org/10.1016/j.jbiomech.2019.05.013
0021-9290/

disturbed flow. Note that the OSI is closely correlated with the formation of the atherosclerotic plaques (Gallo et al., 2016). In addition, the transverse wall shear stress (transWSS) plays a key role in the formation of atherosclerotic plaque (Peiffer et al., 2012; Peiffer et al., 2013). To the authors' knowledge, studies regarding numerical simulation of haemodynamics in the diabetic arteries are rare in the literature. A recent study by Pinello et al. (Schierz et al., 2018) investigated haemodynamics of the diabetic mothers and babies by aid of echo- and electro-cardiography, showing that maternal DM impaired neonatal transitional haemodynamics. Khansari et al. (2017) investigated conjunctival microvascular haemodynamics in stages of the diabetic microvasculopathy. These authors measured several haemodynamic descriptors and suggested that the WSS was identified as a potential marker of the diabetic microvasculopathy. Mora-Gutiérrez et al. (2017) utilized MRI to measure haemodynamic changes in human diabetic nephropathy, suggesting early renal haemodynamic impairment in DM. Another study (Chytilova et al., 2009) suggested that the type 2 DM subjects had lower wall shear rate in carotid arteries than the control ones. However, none of the above-mentioned studies has used numerical simulation to analyze haemodynamics in the diabetic arteries. Thus, changes in haemodynamic parameters due to DM remain largely unclear.

The aim of this study is to investigate changes in haemodynamic parameters of the rabbit descending aortas in response to DM. The type I diabetic rabbit model is raised by injection of alloxan. By aid of CT scanning we reconstruct the three-dimensional realistic models of the non-diabetic and the diabetic rabbit aortas. Using ultrasound measurements and computational tools in biomechanics, the key haemodynamic parameters such as TAWSS, OSI, and transWSS will be computed and analyzed for each rabbit aorta. These numerical data will provide us with a more comprehensive understanding of the potential effects of haemodynamics in high blood glucose on the growth & remodeling (G&R) of the descending aortas.

2. Materials and methods

2.1. Animal model

The process of raising a diabetic rabbit model has been described in a previous study. (Fu et al., 2016; Tong et al., 2018) In brief, ten New Zealand white rabbits, 7 weeks old weighing 1.6–2.2 kg, were purchased from the Experimental Animal Center of Tongji University, Shanghai, China. The rabbits were randomly assigned into two groups, i.e. control and diabetic groups. Each group contains five rabbits. The diabetic group was then injected by 5% solution of alloxan monohydrate dissolved in sterile sodium chloride (100 mg/kg of body weight) to raise a diabetic rabbit model, while the control group was given equal amount of normal saline (0.9% w/v of NaCl). The fasting blood glucose (FBG) was measured 72 h later and the rabbits with FBG level more than 15 mmol/L were considered to be diabetic. If FBG level failed to exceed 15 mmol/L, the rabbits would be further injected by alloxan (130 mg/kg of body weight) until the FBG level was reached. The rabbits were exposed to diabetic condition (i.e. the FBG level over 15 mmol/L) for four weeks prior to CT scanning and measurement of flow velocity waveforms. All experimental procedures complied with international guidelines for care and use of laboratory animals and were approved by the Animal Ethics Committee of Tongji University, Shanghai, China.

2.2. CT scan and flow waveform measurements

To perform CT scanning, 20% of urethane solution was injected into rabbits through ear vein (5 ml/kg). The rabbits after anesthesia were connected to the indwelling needle and was injected developer on ear vein (Fig. 1(a)). The developer was fludeoxyglucose (18F-FDG) with dose of 8 ml and the injection speed was maintained at 0.7 ml/s. (Benz et al., 2017) The layer thickness was set to be 0.5 mm and the scanning was performed on AquilionTM VISION 64 channel spiral CT machine (Toshiba, Japan) in the Department of Radiology at Shanghai East Hospital. As shown in Fig. 1(b), the raw image data of the entire rabbit was then obtained from CT scanning.

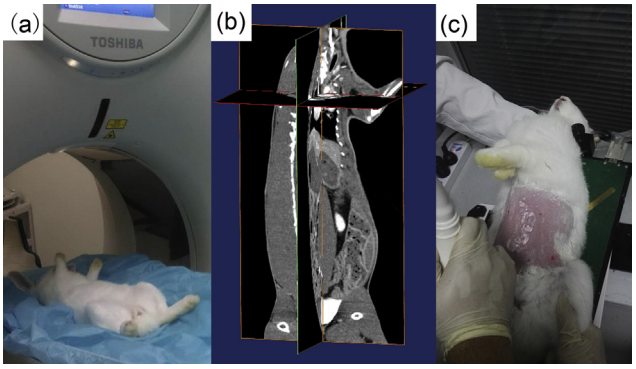

Fig. 1. Representative photograph of (a) a rabbit prepared to CT scanning after anesthesia, (b) three-dimensional CT scanning image of an entire rabbit, and (c) measuring the flow velocity waveforms of the diabetic rabbit aorta using ultrasound machine.

The flow velocity waveforms in the rabbit aortas were measured using the color Doppler ultrasound machine (Vevo2100, VisualSonics Co. Ltd, Toronto Canada). Using depilatory cream, the rabbit abdominal hair was erased. The rabbits were fixed on the ultrasound platform to smear the medical ultrasonic couplant (Fig. 1(c)). Subsequently, we adjusted detection frequency of ultrasonic probe to acquire blood flow velocity waveforms. The measured location was approximately 2–3 cm above the celiac artery.

2.3. 3D reconstruction of aortic geometry

The CT images were imported into the Mimics software (Mimics 15.0 Materialise, Ann Arbor, MI, USA) to reconstruct three-dimensional model of the rabbit descending aorta. First, we established new masks for the descending aorta according to corresponding threshold values (Fig. 2(a)). The redundant parts were erased to form the three-dimensional model of the descending aorta and then we smoothed the model preliminarily. The distance to the celiac artery in the previous ultrasound measurements was used to identify the cutoff point of the inlet based on the reconstructed 3D model. The relevant inlet and outlets of the aorta were cut off based on the centreline. The rabbit descending aorta had one inlet and six major branches as outlets, i.e. celiac artery, cranial mesenteric artery, left and right renal arteries, and two iliac arteries (Barakat et al., 1997). The geometric model was imported into 3-matic software (3-matics 7.0 Materialise, Ann Arbor, MI, USA) to perform local smoothing and the smoothing diameter was set to be 0.5 mm. Subsequently, the accomplished geometric model, as shown in Fig. 2(b), was imported into Solidworks (Dassault Systems S.A, USA) to lengthen the inlet and outlets. The inlet was extended by 30 mm, while the outlets at celiac artery, cranial mesenteric artery, right and left renal arteries were extended by 8 mm. The outlets of two iliac arteries were extended by 15 mm respectively to satisfy the computational inlet and outlet boundary conditions while ensuring smooth entry (see Fig. 2(c)) (Ene-Iordache and Remuzzi, 2012; Javadzadegan et al., 2016; Mahalingam et al., 2016).

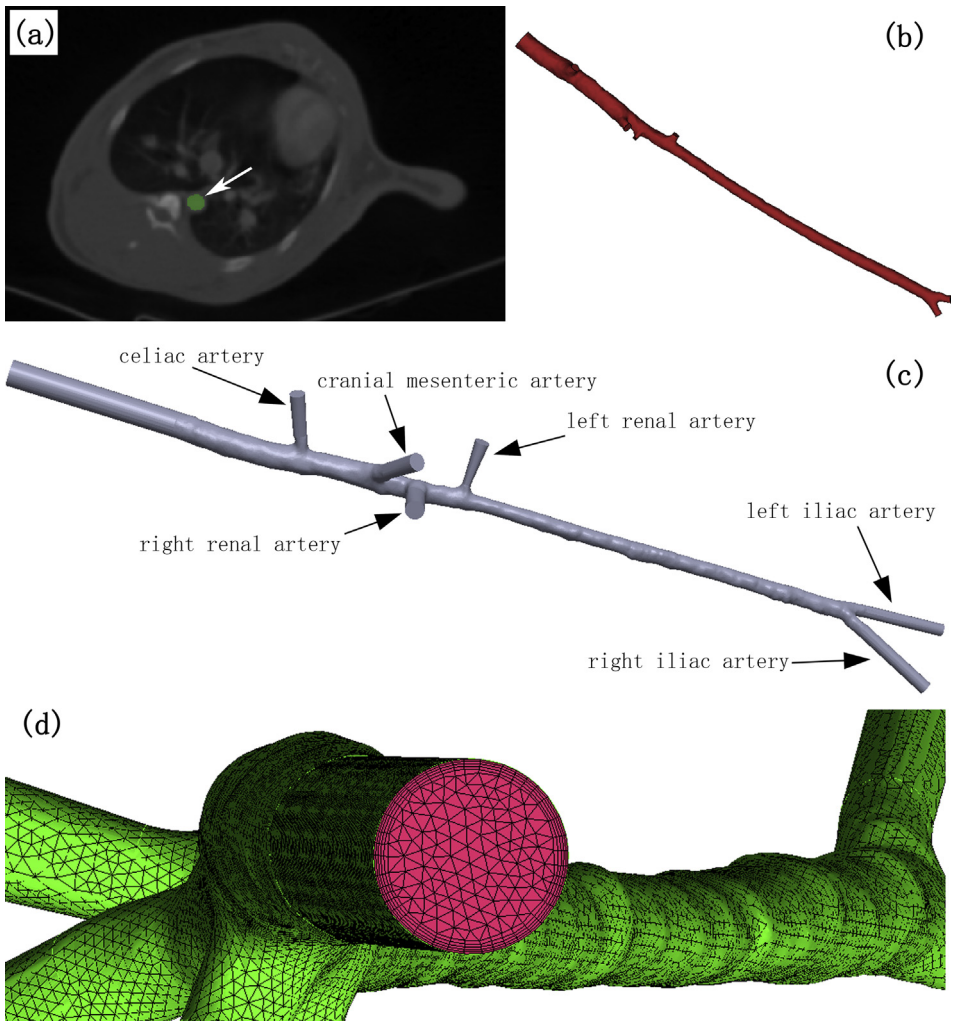

Fig. 2. Representative images of (a) the location of a rabbit descending aorta in the CT scanning, (b) an accomplished rabbit descending aorta model after smoothing, (c) the inlet and outlets of a rabbit descending aorta, and (d) meshed model of the rabbit descending aorta.

The geometric model in Fig. 2(c) was further meshed by the ICEM software (ANSYS, Inc. Canonsburg, PA, USA) with a mixture of tetrahedral and prism volume meshes ranging from 578,947 to 1,259,043 elements (Fig. 2(d)). The maximum elements of inlet, outlet and wall tetrahedral volume meshes were set to be 0.5 mm, 0.2 mm and 0.5 mm, respectively. The boundary layer had the element adjacent to the wall of around 0.02 mm progressively growing over 5 layers to a total thickness of one eighth of the minimum outlet diameter (Li et al., 2017; Mahalingam et al., 2016).

2.4. Governing equation

Blood was modelled as a continuous, homogeneous and incompressible Newtonian fluid (Moore et al., 1994). The blood flow in the rabbit descending aorta was governed by a three-dimensional incompressible Naiver-Stokes equation (Anderson, 2002). Finite element method (FEM) based on commercial software ANSYS (ANSYS 15.0, Inc. Canonsburg, PA, USA) was used to carry out computational analysis (Mahalingam et al., 2016). The CFX was utilized as the solver. The ensemble-averaged governing equations solved for mass and momentum conservation are:

{1} Momentum equation: the momentum equation was based on the momentum conservation principle (Newton's second law) and the general form was written as:

$$\rho\left[\frac{\partial u}{\partial t}+(u\cdot\nabla)u\right]+\nabla p-\mu\nabla^2 u=0, \tag{1}$$

{2} Continuity equation: the continuity equation was based on the mass conservation principle and the general form was written as:

$$\nabla\cdot u=0, \tag{2}$$

where ρ and μ indicated the density and viscosity of blood, respectively. The parameters ρ and μ were often determined to be 1050 $kg\cdot m^{-3}$ and 3.5×10^{-3} $kg\cdot m^{-1}\cdot s^{-1}$ in the literature. (Li et al., 2017) The parameters u and p denoted the three-dimensional velocity vector field and the pressure field in the rabbit descending aorta, respectively.

2.5. Boundary conditions

The flow was assumed as steady and periodical pulsatile volume flow (Alastruey et al., 2009). The measured peak velocities of the non-diabetic and diabetic rabbit aortas were shown in Table 1. The representative flow velocity waveforms based on experimental measurements in the descending aortas of the non-diabetic and the diabetic rabbits were shown in Fig. 3. The velocity waveform of the periodical pulsatile flow was applied to the inlet boundary condition. The maximum Reynolds number was calcu-

Table 1
The measured peak velocities of the non-diabetic (left) and the diabetic (right) rabbit aortas.

Sample number (non-diabetic)	Peak velocity (mm/s)	Sample number (diabetic)	Peak velocity (mm/s)
No. 1	650.86	No. 2	512.13
No. 3	966.35	No. 4	757.76
No. 5	762.00	No. 6	614.52
No. 7	1046.95	No. 8	785.21
No. 9	991.67	No. 10	787.50

lated to be 465 at the inlet (the maximum mean velocity was 384.14 mm/s for all samples). Hence, the flow was simulated as laminar flow. The flow rate percentages of side branches in the rabbit descending aorta were reset according to the flow ratio between each artery branch in the previous experimental measurements (Barakat et al., 1997). In brief, flow splits into the celiac artery was 30.8% of the inflow, 38.1% went into the cranial mesenteric artery, 8.1% went into the right renal artery, 7.2% went into the left renal artery, 7.9% went into one of the iliac arteries and free to the other one. In the present study the aortic wall was assumed as no-slip rigid wall. The equation of distribution of outflow velocity was written as:

$$u_{out} = m \cdot \frac{u_{in} \cdot A_{in}}{A_{out}}, \tag{3}$$

where m was the coefficient of the distribution of different outflows, and A_{in} and A_{out} were the areas of inlet and outlet. Moreover, u_{in} and u_{out} denoted the velocities of inflow and outflow, respectively.

2.6. Haemodynamic indicators

In the present study three haemodynamic parameters, i.e. TAWSS, OSI, and transWSS, were computed by the MATLAB software (MATLAB R2014a Natick, MA, USA). The TAWSS showed the distributions of the wall shear stresses on the aortic wall in one cardiac cycle. The equation was defined as:

$$\mathrm{TAWSS} = \frac{1}{T}\int_0^T |\overrightarrow{\tau_\omega}| dt, \tag{4}$$

where $\overrightarrow{\tau_\omega}$ was the time-dependent WSS vector and T was the cardiac cycle period.

The OSI was used to measure the directional change of WSS during the cardiac cycle and to describe the disturbance of a flow field (Ku et al., 1985). The equation was defined as:

$$\mathrm{OSI} = \frac{1}{2}\left(1 - \frac{\left|\int_0^T \overrightarrow{\tau_\omega} dt\right|}{\int_0^T |\overrightarrow{\tau_\omega}| dt}\right) = \frac{1}{2}\left(1 - \frac{|\overrightarrow{\tau_{mean}}|}{TAWSS}\right), \tag{5}$$

where $\overrightarrow{\tau_{mean}} = \frac{1}{T}\int_0^T \overrightarrow{\tau_\omega} dt$.

The transWSS averaged the transverse components of the instantaneous WSS vectors in a cardiac cycle and was defined as:

$$\mathrm{transWSS} = \frac{1}{T}\int_0^T \left| \overrightarrow{\tau_\omega} \cdot \left(\vec{n} \times \frac{\int_0^T \overrightarrow{\tau_\omega} dt}{\left|\int_0^T \overrightarrow{\tau_\omega} dt\right|} \right) \right| dt, \tag{6}$$

where $\vec{n}$ represented the normal to the arterial surface (Peiffer et al., 2013). The transWSS was used to distinguish between uniaxial pulsatile flow and multidirectional flow, and was regarded as a complement to the traditional haemodynamic metrics like TAWSS and OSI (Li et al., 2017). Note that the transWSS was perpendicular to the mean WSS vector in the plane of the endothelium (Mohamied et al., 2015; Peiffer et al., 2012).

3. Results

3.1. Time-averaged wall shear stress (TAWSS)

The TAWSS distributions of the aortas of five non-diabetic and five diabetic rabbits were shown in Fig. 4. Among these, Fig. 4(a)(c)(e)(g)(i) represented the TAWSS distributions of five individual non-diabetic rabbit aortas, while Fig. 4(b)(d)(f)(h)(j) indicated the corresponding TAWSS distributions of five individual diabetic rabbit aortas.

The distributions of TAWSS in the diabetic rabbit aortas were similar to those in the non-diabetic rabbit aortas. As can be seen from Fig. 4, the red region represented TAWSS values that were greater than 3.96 Pa. We found that the percentage of the TAWSS values that were less than 3.96 Pa accounted for at least over 70% of all the computed TAWSS values for the individual sample. Therefore, we set the regions with the TAWSS values larger than 3.96 Pa to be red, namely the (relatively) high value regions. The mean area percentage of the red regions for the five non-diabetic rabbit aortas was 25.5% (left), while the mean area percentage of the red regions for the five diabetic rabbit aortas was

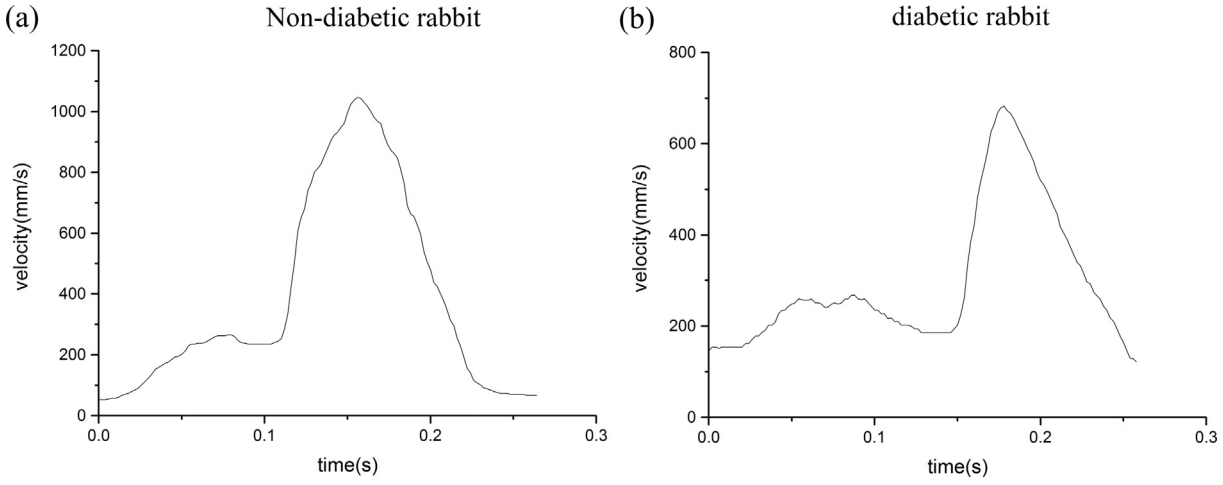

Fig. 3. Representative images of measured flow velocity waveforms in the (a) non-diabetic and the (b) diabetic rabbit aortas.

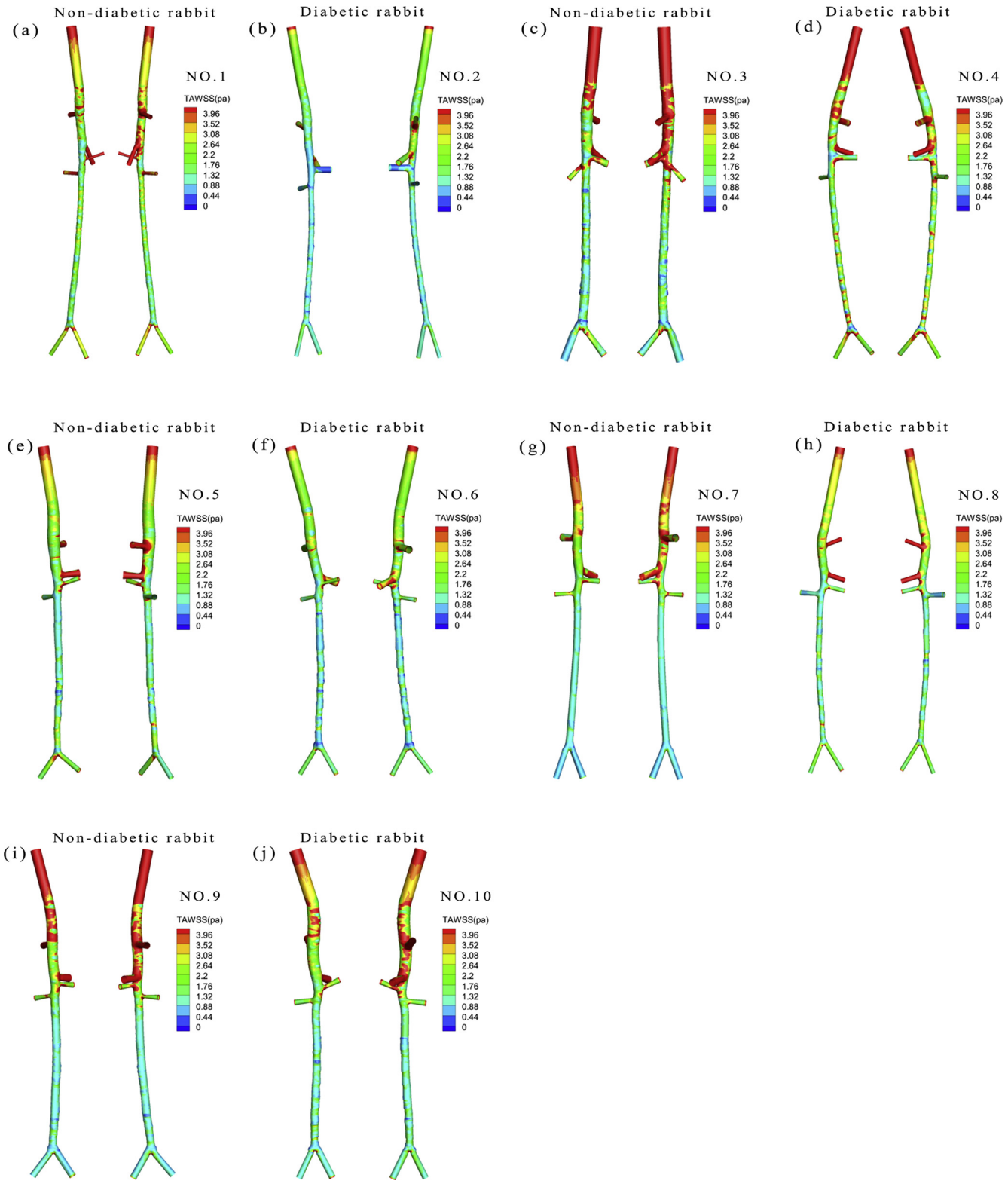

Fig. 4. TAWSS distributions in the (a)(c)(e)(g)(i) five non-diabetic rabbit aortas and the (b)(d)(f)(h)(j) five diabetic rabbit aortas.

15.5% (right). In general, the TAWSS in the diabetic rabbit aortas was lower than that of the non-diabetic rabbit aortas. For all samples, the TAWSS values in the region from inlet to left renal artery were larger than the TAWSS values in the abdominal aorta.

The local TAWSS distributions in the non-diabetic and the diabetic rabbit aortas were representatively shown in Fig. 5(a) and 5(b). It appeared that the TAWSS in the regions A, C, D and region G (i.e. the flank of cranial mesenteric artery) were relatively higher than the other regions such as B, E and F.

3.2. Oscillating shear index (OSI)

The OSI distributions of the non-diabetic and the diabetic rabbit aortas were shown in Fig. 6. In general, the regions

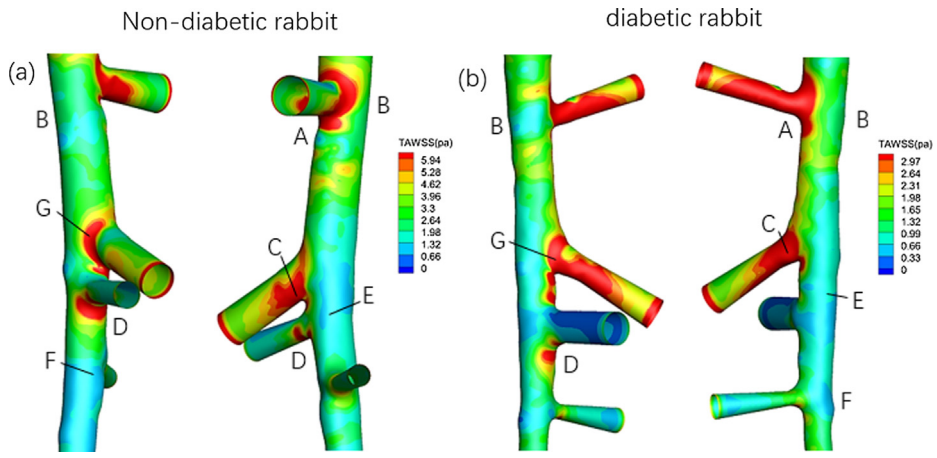

Fig. 5. Representative images of the local TAWSS distributions in the (a) non-diabetic and the (b) diabetic rabbit aortas. The TAWSS in the regions A, C, D and region G (i.e. the flank of cranial mesenteric artery) are relatively higher than the other regions such as B, E and F. By checking the color scale, the TAWSS in the (a) non-diabetic rabbit aortas is higher than that of the (b) diabetic rabbit aortas.

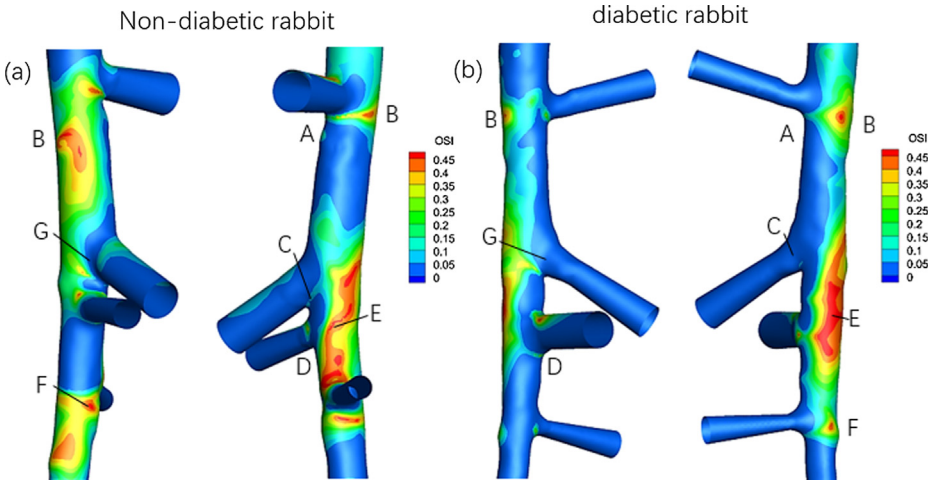

Fig. 6. Representative images of OSI distributions in the (a) non-diabetic and the (b) diabetic rabbit aortas. The OSI in the regions B, E and F are relatively higher than the other regions such as regions A, C and D.

with low TAWSS tended to have high OSI. In particular, the regions B, E and F in the diabetic rabbit aortas tended to have high OSI. In contrast, the regions A, C, D and region G tended to have low OSI.

3.3. Transverse wall shear stress (TransWSS)

Fig. 7 showed the transWSS distributions of the non-diabetic and the diabetic rabbit aortas. We found that the region B tended

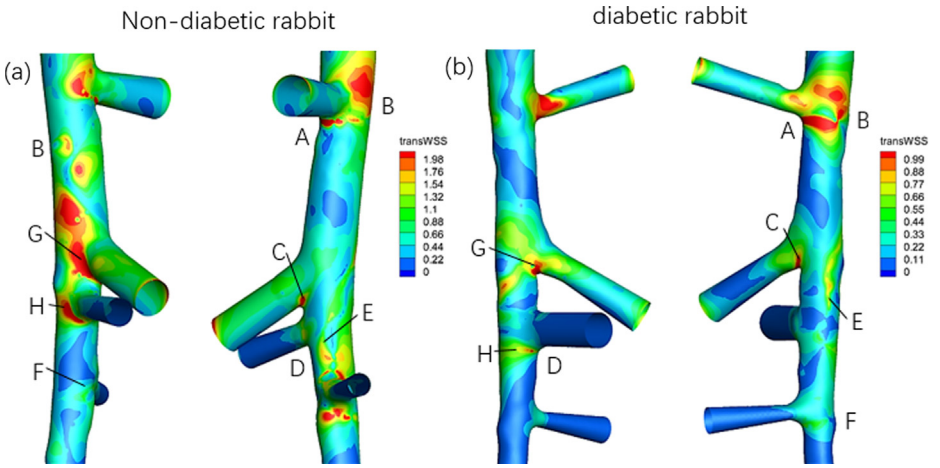

Fig. 7. Representative images of transWSS distributions in the (a) non-diabetic and the (b) diabetic rabbit aortas. The transWSS in the regions B, G and H are relatively higher than the other regions such as D and F. By checking the color scale, the transWSS in the (a) non-diabetic rabbit aortas is higher than that of the (b) diabetic rabbit aortas.

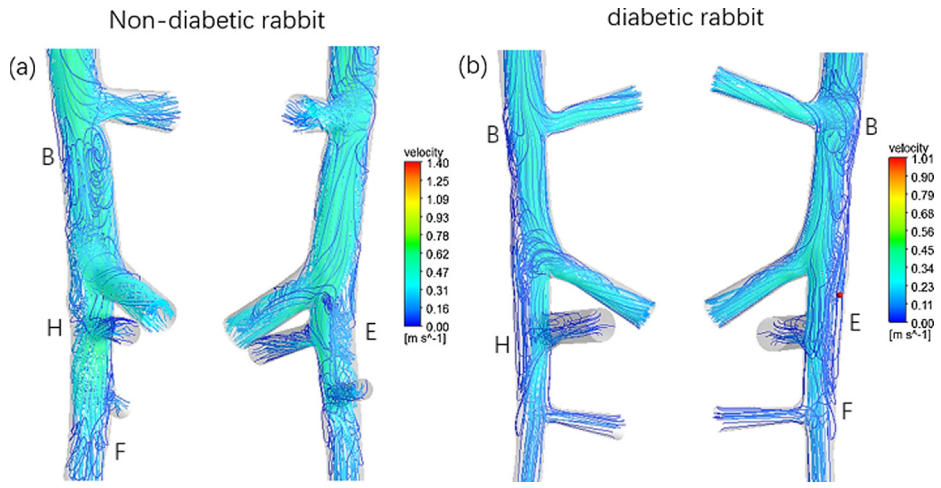

Fig. 8. Representative images of streamlines in the (a) non-diabetic and the (b) diabetic rabbit aortas.

to have high transWSS values in both non-diabetic and diabetic rabbit aortas. For the diabetic rabbit aortas, the region E tended to have (slightly) higher transWSS than the other regions.

3.4. Streamline

Fig. 8 showed streamlines in the non-diabetic and the diabetic rabbit aortas. For the diabetic rabbit aortas, the blood flow generated intense disturbed flow in the regions B, E, H and F. More importantly, these regions tended to have lower flow velocities than the other regions.

3.5. Analysis of haemodynamic parameters

Fig. 9 displayed column plots of the computed haemodynamic parameters in the different regions for five non-diabetic and five diabetic rabbit aortas. Fig. 9(a)(c)(e) showed concrete values in the regions of the non-diabetic rabbit aortas with high TAWSS, OSI and transWSS. Fig. 9(b)(d)(f) showed values in the corresponding regions with high TAWSS, OSI and transWSS for the diabetic rabbit aortas. The TAWSS values were larger than 5 Pa in the regions A, C and D for most rabbit aortas (Fig. 9(a) and 9(b)). Moreover, the regions A and C had higher TAWSS than the region D for both non-diabetic and diabetic rabbit aortas. Notably, the regions A, C and D had high TAWSS values larger than 15 Pa for most non-diabetic rabbit aortas. The TAWSS values of the non-diabetic rabbit aortas were higher than those of the diabetic rabbit aortas except some regions of the sample No. 8 and No. 10. As can be seen from Fig. 9(c) and 9(d), the regions B, E and F had the OSI values larger than 0.4 for most rabbit aortas. The region E had the highest OSI values for all the diabetic rabbit aortas. Fig. 9(e) and 9(f) showed that the regions B, G and H had the transWSS values larger than 1.5 Pa for the non-diabetic rabbit aortas. The transWSS values of the non-diabetic rabbit aortas were higher than those of the diabetic rabbit aortas.

3.6. Statistical analysis

Table 2 showed the mean values of computed haemodynamic parameters for five non-diabetic and five diabetic rabbit aortas in the different regions. The regions A, C and D in the non-diabetic rabbit aortas had significantly higher mean values of TAWSS than the diabetic rabbit aortas ($p = 0.04$). The similar variation trend was also observed for transWSS. The regions B, G and H in the non-diabetic rabbit aortas had significantly higher mean values of transWSS than the diabetic rabbit aortas ($p = 0.02$). There were no significant differences in the mean values of OSI in the regions B, E and F between the non-diabetic and the diabetic rabbit aortas ($p = 0.39$).

4. Discussion

Numerical simulation of haemodynamics is an effective way to advance understanding of the interaction between blood flow and arterial wall (Adib et al., 2017; Filipovic et al., 2012; Lee et al., 2009; Midulla et al., 2012; Moosavi et al., 2014; Qiao et al., 2015; Song et al., 2013). In this study we perform experimental measurements and computational analyses to the non-diabetic and the diabetic rabbit aortas in order to show changes in haemodynamic parameters of the descending aortas in response to DM. The reconstructed three-dimensional aortic model was smoothed in Mimics and the local smoothing was further applied to the model in 3-matics. This method could better keep the original geometry of the lumen. The side branches were artificially prolonged in the present study. The extension tubes could smoothly transform the irregularly-shaped inflow and outflow boundary surfaces into circular-shaped surfaces, and thus, would reduce the influence of the artificial setting of the boundary condition on the numerical results (Liang et al., 2016; Mahalingam et al., 2016). According to flow velocity waveforms based on experimental measurements, we find that blood flow velocities in the non-diabetic rabbit aortas are higher than the velocities in the diabetic rabbit aortas. As a single pathological factor, hyperglycemia may lead to lower blood flow velocities for the diabetic rabbit aortas (Wijngaarden et al., 2017). By observing geometries of all rabbit aortas, there is no remarkable difference between the non-diabetic and the diabetic rabbit aortas. However, the distances between cranial mesenteric artery and two renal arteries are different for individual rabbit aorta. This geometrical feature might affect the distributions of TAWSS.

In general, the bifurcation site is susceptible to high WSS due in large part to changes of flow directions (Wen et al., 2016). The numerical results show that the bifurcation sites of the rabbit descending aortas (i.e. regions A, C, D) tend to have higher TAWSS than the other regions such as B, E, F (Fig. 5). These results are basically consistent with previous numerical simulations in human carotid bifurcation and aortic arch. (Gallo et al., 2016; Lee et al., 2009; Midulla et al., 2012; Wen et al., 2016) It should be emphasized that the rabbit descending aorta has more bifurcations and outlets than carotid artery and aortic arch. Thus, the distribution of TAWSS is more variable for different locations. As can be seen

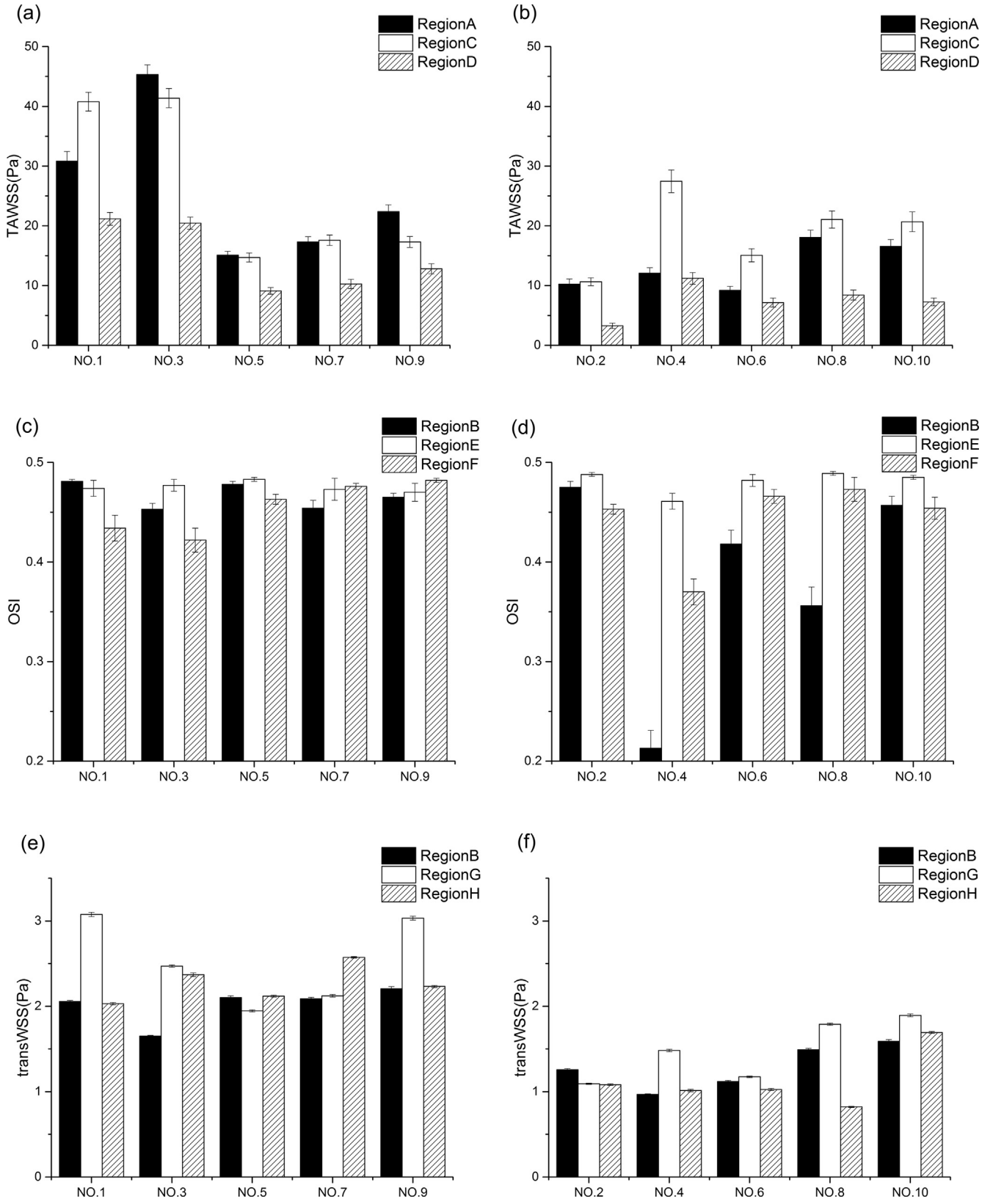

Fig. 9. The quantified values of high TAWSS, OSI and transWSS regions in the (a)(c)(e) non-diabetic and the (b)(d)(f) diabetic rabbit aortas. The TAWSS and transWSS values of the (a)(e) non-diabetic rabbit aortas are higher than those of the (b)(f) diabetic rabbit aortas for most samples. The OSI values in the region E is the highest for some non-diabetic rabbit aortas (c). However, the OSI values in the region E is the highest for all diabetic rabbit aortas (d).

from Fig. 5(a) and (b), the distributions of TAWSS in the non-diabetic rabbit aortas are similar to those in the diabetic rabbit aortas. The mean TAWSS values in the diabetic rabbit aortas are significantly lower than those in the non-diabetic rabbit aortas (Table 2). This can be mainly attributed to the lower velocity of blood stream in the diabetic rabbit aortas.

Table 2
The mean values of computed haemodynamic parameters for five non-diabetic and five diabetic rabbit aortas in the different regions. The regions A, C and D in the non-diabetic rabbit aortas had significantly higher mean values of TAWSS than the diabetic rabbit aortas. The regions B, G and H in the non-diabetic rabbit aortas had significantly higher mean values of transWSS than the diabetic rabbit aortas. The mean values of OSI in the regions B, E and F had no significant differences in the non-diabetic and the diabetic rabbit aortas. However, the region E in the non-diabetic rabbit aortas had lower mean values of OSI than the diabetic rabbit aortas.

TAWSS	Non-diabetic rabbit (Pa) (n = 5)	Diabetic rabbit (Pa) (n = 5)	transWSS	Non-diabetic rabbit (Pa) (n = 5)	Diabetic rabbit (Pa) (n = 5)
Region A	26.191	13.233	Region B	2.020	1.285
Region C	26.348	18.982	Region G	2.530	1.486
Region D	14.766	7.466	Region H	2.266	1.127
p	0.04		*p*	0.02	
OSI	Non-diabetic rabbit (-) (n = 5)	Diabetic rabbit (-) (n = 5)			
Region B	0.466	0.384			
Region E	0.475	0.481			
Region F	0.455	0.443			
p	0.39				

Our numerical results indicate that the back and the flank of aorta outlets (regions B, E, F) tend to have high OSI (see Fig. 6). Compared to the previous studies (Gallo et al., 2016; Midulla et al., 2012; Tong et al., 2018; Wen et al., 2016), the descending aortas have more complicated haemodynamic environment in the back of several artery outlets (e.g., region E). More importantly, the high OSI contributes to the formation of atherosclerotic plaques (Peiffer et al., 2013). Therefore, the regions with high OSI may have a higher propensity of forming the atherosclerotic plaque for the diabetic rabbit aortas. There are no significant differences in the mean values of OSI in the regions B, E and F between the non-diabetic and the diabetic rabbit aortas (Table 2). Thus, changes in the velocities of the diabetic rabbit aortas may not affect the distributions of OSI.

The numerical results, as indicated in Fig. 7, suggest that high transWSS are mainly located at the flank of aorta outlets, i.e. regions B, G, H. We also observe that high transWSS appears in some parts of the regions A and C (see Fig. 7). This phenomenon is consistent with the previous study by Gallo et al. (2016) about haemodynamic analysis in the carotid bifurcation. It suggests that the bifurcation sites tend to have higher transWSS than the other regions. The regions B, G and H in the non-diabetic rabbit aortas have significantly higher mean values of transWSS than the diabetic rabbit aortas (Table 2). This can be attributed to the lower velocities in the diabetic rabbit aortas when compared with the non-diabetic rabbit aortas. It should be also emphasized that there is a correlation between the transWSS and atherosclerotic lesion prevalence (Peiffer et al., 2013). The regions with intense disturbed flow tend to have high OSI (see Figs. 6 and 8). Such a haemodynamic feature has been described in the previous studies (Andersson et al., 2017; Fan et al., 2016; Gallo et al., 2016). Similarly, these studies also indicate that the regions with low TAWSS tend to have high OSI.

For all samples, the back of right renal artery (i.e. region E) tends to have high OSI (Fig. 9). Note that the region E is a special site located in the back of three artery outlets (i.e. the cranial mesenteric artery, the left and the right renal arteries). Therefore, flow in this region may lead to velocity differences. This phenomenon is consistent with the previous numerical simulations in the rabbit aortic arch (Li et al., 2017). In the present study, we find that the region E in the non-diabetic rabbit aortas has lower mean values of OSI than the diabetic rabbit aortas. It suggests that the region E is a location that may be highly susceptible to haemodynamic changes for the diabetic rabbit aortas. As shown in Fig. 9(d), the computed OSI values are high for the diabetic rabbit aortas in the regions B, E, F. In particular, the consistently high OSI values in the region E may contribute to local vascular remodeling in that area. According to the results, we find that the distributions of OSI may not be associated with the values of velocity and WSS. In contrast, differences in the distributions of OSI may be dependent on the aortic geometries.

This study has some limitations. First, some assumptions such as incompressible Newtonian fluid, no-slip aortic wall were included in the simulation to simplify the computational process. These assumptions, however, were frequently used in the haemodynamic simulation in the previous studies (Gallo et al., 2016; Liu et al., 2009; Li et al., 2017; Peiffer et al., 2012; Peiffer et al., 2013; Peiffer et al., 2013). Although a previous study (Lee and Steinman, 2007) suggested that the Newtonian fluid model would not affect the numerical results significantly, the viscosity of blood needs to be measured for the individual rabbit in order to perform a more accurate haemodynamic analysis. The tapering of the descending aorta in the inlet portion is also a very important factor that would substantially influence the imposed inlet velocity and the related numerical results. Second, the rabbit-specific variability in outlet boundary conditions is not modelled. Because the velocities in the side branches of the rabbit aortas were not measured with ultrasound machine in the present study. The main problem is that a large number of intestinal contents that are accumulated in the abdominal cavity of supine rabbits may interfere with the ultrasonic detection. It is difficult to identify the specific location of each side branch along the rabbit aorta and inappropriate location will certainly affect the data measured for each side branch. Currently we are working with experienced cardiologists to optimize the method to measure the velocities in the side branches in a rabbit aorta. Finally, changes in mechanical properties of the diabetic aortas were not considered. A recent study reported that there was pronounced tissue stiffening for the diabetic aortas when compared to the control aortas (Tong et al., 2018). Therefore, we are developing a more sophisticated fluid-structure interaction (FSI) model to investigate haemodynamics of the rabbit aortas in health and diabetes.

5. Conclusion

In the present study the distributions of TAWSS, OSI, and transWSS in the non-diabetic rabbit aortas are similar to those in the diabetic rabbit aortas. However, the mean TAWSS and transWSS values in the non-diabetic rabbit aortas are significantly higher than those in the diabetic rabbit aortas. For both the non-diabetic and the diabetic rabbit aortas, the bifurcation zones tend to have high TAWSS and the flanks of the aorta outlets tend to have high transWSS. In addition, the back of right renal artery tends to have high OSI in the non-diabetic and the diabetic rabbit aortas. Thus, these regions may be susceptible to forming localized aortic wall remodeling. As for future studies, more rabbit aortas are needed to perform both experimental measurements and numerical simulation in order to eliminate individual differences caused

by animal model. Moreover, FSI model will be used in the numerical simulation to provide a more realistic haemodynamic analysis.

Declaration of Competing Interest

None.

Acknowledgements

This work was financially supported by the National Natural Science Foundation of China (Grant No. 11702197, No. 11572064), "Shanghai Pujiang Program" (16PJ1409200), the Fundamental Research Funds for Central Universities (1500219128, 2018CDPTCG0001-10) and Visiting Scholar Foundation of Key Laboratory of Biorheological Science and Technology (Chongqing University), Ministry of Education, P. R. China (CQKLBST-2016-010). The authors particularly thank Mr. Guangxue Wang from Research Center for Translational Medicine, Shanghai East Hospital for his help during the ultrasound data collection and Prof. Fuyou Liang from Shanghai Jiao Tong University for consulting methods in haemodynamic simulation.

References

Adib, M.A.H.M., Li, S., Watanabe, Y., Wada, S., 2017. Minimizing the blood velocity differences between phase-contrast magnetic resonance imaging and computational fuid dynamics simulation in cerebral arteries and aneurysms. Med. Biol. Eng. Comput. 55, 1605–1619.

Akhtar, R., Cruichshank, J.K., Zhao, X., Walton, L.A., Gardiner, N.J., Barrett, S.D., Graham, H.K., Derby, B., Sherratt, M.J., 2014. A Localized micro- and nano-scale remodeling in the diabetic aorta. Acta Biomater. 10, 4843–4851.

Alastruey, J., Nagel, S.R., Nier, B.A., Hunt, A.A.E., Weinberg, P.D., Peiró, J., 2009. Modelling pulse wave propagation in the rabbit systemic circulation to assess the effects of altered nitric oxide synthesis. J. Biomech. 42, 2116–2123.

Anderson, J., 2002. Computational Fluid Dynamics. McGraw-Hill Education, New York.

Andersson, M., Lantz, J., Ebbers, T., Karlsson, M., 2017. Multidirectional WSS disturbances in stenotic turbulent flows: A pre- and post-intervention study in an aortic coarctation. J. Biomech. 51, 8–16.

Bachmann, K.N., Wang, T., 2018. Biomarkers of cardiovascular disease: contributions to risk prediction in individuals with diabetes. Diabetologia 61, 987–995.

Barakat, A.I., Marini, R.P., Colton, C.K., 1997. Measurement of flow rates through aortic branches in the anesthetized rabbit. Lab. Anim. Sci. 47, 184–189.

Beckman, J.A., Creager, M.A., Libby, P., 2002. Diabetes and atherosclerosis: epidemiology, pathophysiology and management. JAMA 287, 2570–2581.

Benz, M.R., Szucs-Farkas, Z., Froehlich, J.M., Stadelmann, G., Bongartz, G., Bouwman, L., Schindera, S.T., 2017. Scan time adapted contrast agent injection protocols with low volume for low-tube voltage CT angiography: an in vitro study. Eur. J. Radiol. 93, 65–69.

Caro, C.G., Fitzgerald, J.M., Schroter, R.C., 1971. Atheroma and arterial wall shear observation, correlation and proposal of a shear dependent mass transfer mechanism for atherogenesis. Proc. R. Soc. Lond. B Biol. Sci. 177, 109–159.

Casanova, F., Adingupu, D.D., Adams, F., Gooding, K.M., Looker, H.C., Aizawa, K., Dove, F., Elyas, S., Belch, J.J.F., Gates, P.E., Littleford, R.C., Gilchrist, M., Colhoun, H.M., Shore, A.C., Khan, F., Strain, W.D., 2017. The impact of cardiovascular co-morbidities and duration of diabetes on the association between microvascular function and glycaemic control. Cardiovasc. Diabetol. 16, 114.

Chytilova, E., Malik, J., Kasalova, Z., Dolezalova, R., Stulc, T., Ceska, R., 2009. Lower wall shear rate of the common carotid artery in treated type 2 diabetes mellitus with metabolic syndrome. Physiol. Res. 58, 185–191.

Ene-Iordache, B., Remuzzi, A., 2012. Disturbed flow in radial-cephalic arteriovenous fistulae for haemodialysis: low and oscillating shear stress locates the sites of stenosis. Nephrol. Dial. Transplant. 27, 358–368.

Fan, T., Lu, Y., Gao, Y., Meng, J., Tan, W., Huo, Y., Kassab, G.S., 2016. Hemodynamics of left internal mammary artery bypass graft: Effect of anastomotic geometry, coronary artery stenosis, and postoperative time. J. Biomech. 49, 645–652.

Feng, X., Liang, L., Wu, J., Chen, Y., Liang, S., 2017. 64-Slice spiral double-low CT to evaluate the degree of stenosis and plaque composition in diagnosing coronary artery disease. Exp. Ther. Med. 14, 3088–3092.

Filipovic, N., Rosic, M., Tanaskovic, I., Milosevic, Z., Nikolic, D., Zdravkovic, N., Peulic, A., Kojic, M.R., Fotiadis, D.I., Parodi, O., 2012. ARTreat Project: Three-dimensional numerical simulation of plaque formation and development in the arteries. IEEE Trans. Inf. Technol. Biomed. 16, 272–278.

Fu, H., Li, G., Liu, C., Li, J., Cheng, L., Yang, W., Tse, G., Zhao, J., Liu, T., 2016. Probucol prevents atrial ion channel remodeling in an alloxan-induced diabetes rabbit model. Oncotarget 7, 83850–83858.

Gallo, D., Steinman, D.A., Morbiducci, U., 2016. Insights into the co-localization of magnitude-based versus direction-based indicators of disturbed shear at the carotid bifurcation. J. Biomech. 49, 2413–2419.

Javadzadegan, A., Lotfi, A., Simmons, A., Barber, T., 2016. Haemodynamic analysis of femoral artery bifurcation models under different physiological flow waveforms. Comput. Methods Biomech. Biomed. Eng. 19, 1143–1153.

Khansari, M.M., Wanek, J., Tan, M., Joslin, C.E., Kresovich, J.K., Camardo, N., Blair, N. P., Shahidi, M., 2017. Assessment of conjunctival microvascular hemodynamics in stages of diabetic microvasculopathy. Sci. Rep. 7, 45916.

Ku, D.N., Giddens, D.P., Zarins, C.K., Glagov, S., 1985. Pulsatile flow and atherosclerosis in the human carotid bifurcation. Positive correlation between plaque location and low oscillating shear stress. Arteriosclerosis 5, 293–302.

Lee, S.W., Antiga, L., Steinman, D.A., 2009. Correlations among indicators of disturbed flow at the normal carotid bifurcation. J. Biomech. Eng. 131, 309–321.

Lee, S.W., Steinman, D.A., 2007. On the relative importance of rheology for image-based CFD models of the carotid bifurcation. J. Biomech. Eng. 129, 273–278.

Lehman, S.J., Schlett, C.L., Bamberg, F., Lee, H., Donnelly, P., Shturman, L., Kriegel, M. F., Brady, T.J., Hoffmann, U., 2009. Assessment of coronary plaque progression in coronary CT angiography using a semi-quantitative score. JACC Cardiovasc. Imaging 2, 1262–1270.

Liang, F., Liu, X., Yamaguchi, R., Liu, H., 2016. Sensitivity of flow patterns in aneurysms on the anterior communicating artery to anatomic variations of the cerebral arterial network. J. Biomech. 49, 3731–3740.

Liu, X., Pu, F., Fan, Y., Deng, X., Li, D., Li, S., 2009. A numerical study on the flow of blood and the transport of LDL in the human aorta: the physiological significance of the helical flow in the aortic arch. Am. J. Physiol. Heart Circ. Physiol. 297, H163–170.

Li, X., Liu, X., Zhang, P., Feng, C., Sun, A., Kang, H., Deng, X., Fan, Y., 2017. Numerical simulation of haemodynamics and low-density lipoprotein transport in the rabbit aorta and their correlation with atherosclerotic plaque thickness. J. R. Soc. Interface 14, 20170140.

Mahalingam, A., Gawandalkar, U.U., Kini, G., Buradi, A., Araki, T., Ikeda, N., Nicolaides, A., Laird, J.R., Saba, L., Suri, J.S., 2016. Numerical analysis of the effect of turbulence transition on the hemodynamic parameters in human coronary arteries. Cardiovasc. Diagn. Ther. 6, 208–220.

Malek, A.M., Alper, S.L., Izumo, S., 1999. Hemodynamic shear stress and its role in atherosclerosis. JAMA 282, 2035–2042.

Midulla, M., Moreno, R., Baali, A., Chau, M., Negre-Salvayre, A., Nicoud, F., Pruvo, J.P., Haulon, S., Rousseau, H., 2012. Haemodynamic imaging of thoracic stent-grafts by computational fluid dynamics (CFD): presentation of a patient-specific method combining magnetic resonance imaging and numerical simulations. Eur. Radiol. 22, 2094–2102.

Mohamied, Y., Rowland, E.M., Bailey, E.L., Sherwin, S.J., Schwartz, M.A., Weinberg, P. D., 2015. Change of direction in the biomechanics of atherosclerosis. Ann. Biomed. Eng. 43, 16–25.

Moore Jr, J.E., Maier, S.E., Ku, D.N., Boesiger, P., 1994. Hemodynamics in the abdominal aorta: a comparison of in vitro and in vivo measurements. J. Appl. Physiol. 76, 1520–1527.

Moosavi, M.H., Fatouraee, N., Katoozian, H., Pashaei, A., Camara, O., Frangi, A.F., 2014. Numerical simulation of blood flow in the left ventricle and aortic sinus using magnetic resonance imaging and computational fluid dynamics. Comput. Methods Biomech. Biomed. Eng. 17, 740–749.

Mora-Gutiérrez, J.M., Garcia-Fernandez, N., Slon Roblero, M.F., Páramo, J.A., Escalada, F.J., Wang, D.J.J., Benito, A., Fernández-Seara, M.A., 2017. Arterial spin labeling MRI is able to detect early hemodynamic changes in diabetic nephropathy. J. Magn. Reson. Imaging 46, 1810–1817.

Peiffer, V., Weinberg, P.D., Sherwin, S.J., 2012. The wall shear stress vector: methods for characterising truly disturbed flow. In: ASME 2012 Summer Bioengineering Conference. American Society of Mechanical Engineers, pp. 21–22.

Peiffer, V., Sherwin, S.J., Weinberg, P.D., 2013. Computation in the rabbit aorta of a new metric–the transverse wall shear stress–to quantify the multidirectional character of disturbed blood flow. J. Biomech. 46, 2651–2658.

Peiffer, V., Sherwin, S.J., Weinberg, P.D., 2013. Does low and oscillatory wall shear stress correlate spatially with early atherosclerosis? A Syst. Rev. Cardiovasc. Res. 99, 242–250.

Qiao, A., Yin, W., Chu, B., 2015. Numerical simulation of fluid–structure interaction in bypassed DeBakey III aortic dissection. Comput. Methods Biomech. Biomed. Eng. 18, 1173–1180.

Schierz, I.A.M., Pinello, G., Piro, E., Giuffrè, M., Placa, S.L., Corsello, G., 2018. Transitional hemodynamics in infants of diabetic mothers by targeted neonatal echocardiography, electrocardiography and peripheral flow study. J. Matern. Fetal Neonatal. Med. 31, 1578–1585.

Seftel, A.D., 2017. Re: Testosterone treatment and coronary artery plaque volume in older men with low testosterone. J. Urol. 198, 727–728.

Song, K., Wang, H., Zhang, B., Lim, M., Liu, Y., Liu, T., 2013. Numerical simulation of fluid field and in vitro three-dimensional fabrication of tissue-engineered bones in a rotating bioreactor and in vivo implantation for repairing segmental bone defects. Cell Stress Chaperones 18, 193–201.

Tong, J., Yang, F., Li, X., Xu, X., Wang, G., 2018. Mechanical characterization and material modeling of diabetic aortas in a rabbit model. Ann. Biomed. Eng. 46, 429–442.

Wen, J., Yuan, D., Wang, Q., Hu, Y., Zhao, J., Zheng, T., Fan, Y., 2016. A computational simulation of the effect of hybrid treatment for thoracoabdominal aortic aneurysm on the hemodynamics of abdominal aorta. Sci. Rep. 6, 23801.

Wijngaarden, R.P.T., Overbeek, J.A., Heintjes, E.M., Schubert, A., Diels, J., Straatman, H., Steyerberg, E.W., Herings, R.M.C., 2017. Relation between different measures

of glycemic exposure and microvascular and macrovascular complications in patients with type 2 diabetes mellitus: an observational cohort study. Diabetes Ther. 8, 1097–1109.

Xu, X., Geng, H., Zhang, Q., Yu, J., Chu, Y., Dong, G., Wu, J., 2018. Investigation of 3D reduced field of view carotid atherosclerotic plaque imaging. Magn. Reson. Imaging 49, 10–15.

Zhao, X., Li, R., Hippe, D.S., Hatsukami, T.S., Yuan, C., 2017. Chinese Atherosclerosis Risk Evaluation (CARE II) study: a novel cross-sectional, multicentre study of the prevalence of high-risk atherosclerotic carotid plaque in Chinese patients with ischaemic cerebrovascular events-design and rationale. Stroke Vasc. Neurol. 2, 15–20.